Journal of Science and Technology in Civil Engineering, HUCE, 2025

A CS-MITC3+ PLATE ELEMENT FOR STATIC ANALYSIS OF HSDT-TYPE FUNCTIONALLY GRADED PLATES UNDER THERMO-MECHANICAL LOADING

Thanh Chau-Dinh[a,*], Minh La-Tuan[b], Binh Le-Phuong[a]

[a]*Faculty of Civil Engineering, Ho Chi Minh City University of Technology and Education, 01 Vo Van Ngan street, Thu Duc ward, Ho Chi Minh city, Vietnam*
[b]*Office of People's Council and People's Committee at Chau Doc Ward, 12 Le Loi street, Chau Doc ward, An Giang province, Vietnam*

Article history:
Received 08/4/2025, Revised 11/5/2025, Accepted 30/5/2025

Abstract

This paper introduces the development of a 3-node triangular plate element, which utilizes C^0-type shape functions enhanced by a cubic function at the bubble node positioned at the element's centroid. This element is designed for the static analysis of functionally graded (FG) plates based on high-order shear deformation theory (HSDT). The in-plane strains of the element are averaged over sub-triangular domains bounded by straight lines connecting the vertex nodes to the bubble node. The cell-based smoothed (CS) technique simplifies the integration of in-plane stiffness matrices by confining it to the boundaries of the sub-triangular domains. To reduce the shear-locking phenomenon caused by the thin plate's thickness, the approach of mixed interpolation tensorial components (MITC3+) is employed to independently interpolate the transverse shear strains. Several benchmark FG plates subjected to thermo-mechanical loading are statically analyzed using the proposed element, referred to as the CS-MITC3+ plate element. The robustness of the presented element is evaluated in comparison with references.

Keywords: FG plates; HSDT; CS-FEM; MITC3+; thermo-mechanical loading.

1. Introduction

Functionally graded (FG) plates, originating from functionally graded materials first proposed by Japanese scientists in 1984 during a space exploration research project [1], are composed of two distinct materials: ceramic on the top side and metal on the bottom side in order that their material properties continuously vary along the thickness direction. The FG plates avoid stress concentration and combine the advantages of ceramics, such as excellent thermal insulation and wear resistance, with the durability, ductility, and fatigue resistance of metals. Due to these superior properties, FG plates are increasingly being applied in various fields.

Analyzing FG plates necessitates the development of analytical theories and solution methods to accurately predict their responses, considering arbitrary shapes, boundary conditions, and loads. The classical Kirchhoff plate theory [2] is applicable to thin FG plates as it neglects transverse shear strains. In contrast, the shear deformation theories, which account for transverse shear strains, are suitable for thick FG plates. The first-order shear deformation theory (FSDT) of Reissner [3] and Mindlin [4] assumes that the transverse shear strains are constant through the plate's thickness and requires a shear correction factor to adjust the transverse shear strain energy. To capture the variation of transverse shear strains through the thickness, especially ensuring their zero values at the bottom

*Corresponding author. *E-mail address:* chdthanh@hcmute.edu.vn (Chau-Dinh, T.)

and top planes of the plate, numerous higher-order shear deformation theories (HSDT) have been developed to enhance the analysis of FG plates [5–10].

Over the past decades, various analytical and numerical methods have been proposed to solve the problem of FG plates. Among these, the finite element method (FEM) has been the most widely used and advantageous due to its ability to handle FG plates of any shape, with varied boundary conditions and loads. The simplest formulations of plate elements are the 3-node triangular elements, derived from C^0-type displacement approximations and shear deformation theories. These 3-node triangular plate elements remain the most conventional choice for modeling plates with complex geometries. However, the 3-node triangular plate elements using the C^0-type approximation functions cannot represent the transverse shear strains as zero, which corresponds to the actual behavior of thin plate structures. This leads to the shear deformation energy of these elements exceeding the actual shear deformation energy as the plate thickness becomes thinner. This phenomenon is referred to as shear locking. To overcome the phenomenon of shear locking, various methods have been suggested for 3-node triangular plate elements such as the Mindlin-type (MIN3) [11], Discrete Shear Gap (DSG3) [12] or Mixed Interpolation of Tensorial Components (MITC3) [13].

Moreover, the strain and stress fields of plates modeled using standard C^0-type 3-node triangular plate elements remain constant within each individual element. To minimize the strain differences between elements, the strain fields of elements are averaged on sub-domains defined by elements sharing common edges, common nodes, or sub-triangular domains achieved by connecting vertex nodes to bubble nodes. These approaches are respectively demonstrated in the Edge-based Smoothed (ES-), Node-based-Smoothed (NS-) or Cell-based Smoothed (CS-) FEM of the Smoothed FEM (S-FEM) [14]. The smoothed strain techniques have been proposed for shear-locking free 3-node triangular plate elements, such as DSG3, MITC3, and MIN3, to analyze FG plates [15–20]. Alternatively, Lee et al. [21] introduced an enriched C^0-type interpolation by incorporating a cubic shape function at the bubble node positioned at the centroid of the 3-node triangular plate element, and developed a shear-locking removal technique known as MITC3+. The MITC3+ plate element was first introduced with the CS technique in [22] to study the behaviors of isotropic plates under static loads. In comparison with the ES or NS techniques, which search elements having common edges or nodes for smoothed domains, the CS technique is straightforwardly implemented in the loop of element stiffness computation, resulting in saved computational time. Therefore, this study suggests using the MITC3+ plate element, improved by the CS technique, to analyze FG plates under thermo-mechanical loading based on the third-order shear deformation theory.

In the next section, the HSDT-type behaviors of FG plates are briefly presented, followed by a detailed derivation of the formulation of the proposed 3-node triangular plate element. The accuracy and efficiency of the suggested element are assessed through several benchmark FG plates in Section 3. Finally, conclusions are drawn in the last section.

2. Formulation of CS-MITC3+ plate element for higher-order shear deformation theory of functionally graded plates

Although many functionally graded distributions, such as sandwich, bi-directional or tri-directional FG materials [19, 23–25], have been proposed, this research focuses on one-directional FG plates composed of metal and ceramic, where the FG material properties gradually change from metal at the bottom plane to ceramic at the top plane. The Young's modulus $E(z)$, coefficients of thermal conduction $k(z)$ and expansion $\alpha(z)$ of the FG plates vary through the thickness by the power law [5] as

follows

$$E(z) = (E_c - E_m)\left(\frac{2z+t}{2t}\right)^n + E_m$$
$$k(z) = (k_c - k_m)\left(\frac{2z+t}{2t}\right)^n + k_m; \quad \alpha(z) = (\alpha_c - \alpha_m)\left(\frac{2z+t}{2t}\right)^n + \alpha_m \tag{1}$$

where E_m, k_m, α_m and E_c, k_c, α_c are respectively the Young's moduli, thermal conduction and expansion coefficients of the metal and ceramic; t is the plate's thickness; n is the power law index; z is the axis of the Cartesian coordinate system $Oxyz$ in which Oxy locates on the middle plane of the plate as shown in Fig. 1. The Poisson's ratio $\nu(z)$ is assumed to be constant.

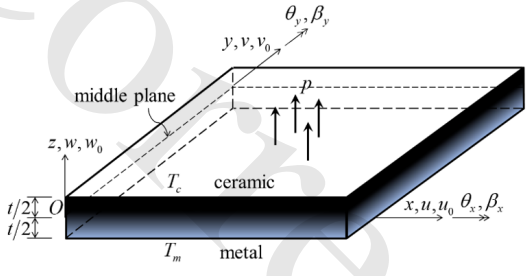

Figure 1. Geometry of FG plate with positive directions of the displacement fields

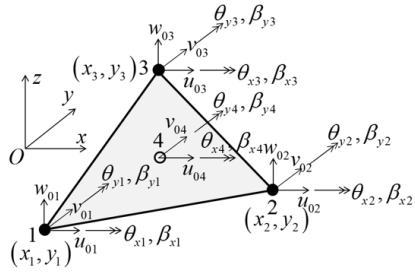

Figure 2. Positive sign conventions of dofs of presented element

The FG plates are subjected to transverse distributed load p, and temperature T_m at the bottom and T_c at the top. The temperature $T(z)$ varying through thickness is determined by the one-dimensional Fourier equation of heat conduction [26]

$$\frac{\mathrm{d}}{\mathrm{d}z}\left[k(z)\frac{\mathrm{d}T(z)}{\mathrm{d}z}\right] = 0 \text{ with } T(z=-t/2) = T_m, T(z=t/2) = T_c \tag{2}$$

Solving Eq. (2) gives

$$T(z) = T_m + (T_c - T_m)\left(\frac{2z+t}{2t}\right)\frac{\sum_{q=0}^{\infty}\left[-\left(\frac{2z+t}{2t}\right)^n\frac{k_c-k_m}{k_m}\right]^q/(nq+1)}{\sum_{q=0}^{\infty}\left(-\frac{k_c-k_m}{k_m}\right)^q/(nq+1)} \tag{3}$$

and the first 7 terms of the series (3) are enough convergence to obtain $T(z)$.

According to the higher-order shear deformation theory [27], the displacement fields u, v, w in the x-, y-, z-directions respectively of the FG plates are

$$u = u_0 + z\theta_y - \frac{4z^3}{3t^2}\left(\theta_y + \beta_y\right); \quad v = v_0 - z\theta_x + \frac{4z^3}{3t^2}\left(\theta_x + \beta_x\right); \quad w = w_0 \tag{4}$$

in which u_0, v_0, w_0, θ_x and θ_y are the translational and rotational displacements of middle plane with their directions and senses defined in Fig. 1; and $\beta_x = \partial w/\partial x, \beta_y = \partial w/\partial y$.

From the displacement fields in Eq. (4), the strain fields are determined by

$$\boldsymbol{\varepsilon} = \begin{bmatrix}\varepsilon_x & \varepsilon_y & \gamma_{xy}\end{bmatrix}^T = \boldsymbol{\varepsilon}_m + z\boldsymbol{\varepsilon}_b + z^3\boldsymbol{\varepsilon}_\kappa; \quad \boldsymbol{\gamma} = \begin{bmatrix}\gamma_{xz} & \gamma_{yz}\end{bmatrix}^T = \boldsymbol{\gamma}_0 + z^2\boldsymbol{\gamma}_1$$
$$\boldsymbol{\varepsilon}^{th} = \begin{bmatrix}\varepsilon_x^{th} & \varepsilon_y^{th} & \gamma_{xy}^{th}\end{bmatrix}^T = \alpha(z)\Delta T(z)\begin{bmatrix}1 & 1 & 0\end{bmatrix}^T \text{ with } \Delta T(z) = T(z) - T_m \tag{5}$$

where

$$\begin{aligned}
&\boldsymbol{\varepsilon}_m = \begin{bmatrix} u_{0,x} & v_{0,y} & u_{0,y} + v_{0,x} \end{bmatrix}^T; \quad \boldsymbol{\varepsilon}_b = \begin{bmatrix} \theta_{x,x} & \theta_{y,y} & \theta_{x,y} + \theta_{y,x} \end{bmatrix}^T \\
&\boldsymbol{\varepsilon}_\kappa = c\begin{bmatrix} \theta_{x,x} + \beta_{x,x} & \theta_{y,y} + \beta_{y,y} & \theta_{x,y} + \theta_{y,x} + \beta_{x,y} + \beta_{y,x} \end{bmatrix}^T \\
&\boldsymbol{\gamma}_0 = \begin{bmatrix} \theta_x + w_{0.x} & \theta_y + w_{0.y} \end{bmatrix}^T; \quad \boldsymbol{\gamma}_1 = 3c\begin{bmatrix} \theta_x + \beta_x & \theta_y + \beta_y \end{bmatrix}^T
\end{aligned} \tag{6}$$

with $c = -4/(3t^2)$ and the subscript commas denote derivatives.

The stress fields are computed from the strain fields in Eq. (5) as follows

$$\boldsymbol{\sigma} = \begin{bmatrix} \sigma_x & \sigma_y & \tau_{xy} \end{bmatrix}^T = \mathbf{E}\left(\boldsymbol{\varepsilon} - \boldsymbol{\varepsilon}^{th}\right); \quad \boldsymbol{\tau} = \begin{bmatrix} \tau_{xz} & \tau_{yz} \end{bmatrix}^T = \mathbf{G}\boldsymbol{\gamma} \tag{7}$$

with

$$\mathbf{E}(z) = \frac{E(z)}{1-\nu(z)^2}\begin{bmatrix} 1 & \nu(z) & 0 \\ \nu(z) & 1 & 0 \\ 0 & 0 & [1-\nu(z)]/2 \end{bmatrix}; \quad \mathbf{G}(z) = \frac{E(z)}{2[1-\nu(z)]}\begin{bmatrix} 1 & 0 \\ 0 & 1 \end{bmatrix} \tag{8}$$

2.1. MITC3+ plate element for HSDT-type FG plates

To solve the behaviors of the FG plates based on the HSDT, the displacement fields given in Eq. (4) are approximated by those of 3-node triangular plate elements expressed by

$$\begin{aligned}
&u_0 = \sum_{I=1}^{4} H_I u_{0I}; \quad v_0 = \sum_{I=1}^{4} H_I v_{0I}; \quad w_0 = \sum_{I=1}^{4} H_I w_{0I} \\
&\theta_x = \sum_{I=1}^{4} H_I \theta_{xI}; \quad \theta_y = \sum_{I=1}^{4} H_I \theta_{yI}; \quad \beta_x = \sum_{I=1}^{4} H_I \beta_{xI}; \quad \beta_y = \sum_{I=1}^{4} H_I \beta_{yI}
\end{aligned} \tag{9}$$

where u_{0I}, v_{0I}, w_{0I}, θ_{xI}, θ_{yI} are the displacements of node I with $w_{04} = 0$; β_{xI}, β_{yI} are the warping of node I used to interpolate β_x, β_y independently from the derivatives of deflection $\beta_x = \partial w/\partial x$ and $\beta_y = \partial w/\partial y$ [28], in which the positive sign conventions of the 7 degrees of freedom (dofs) at each node of the 3-node triangular plate element with a bubble node are defined in Fig. 2; and H_I are the shape functions including a cubic bubble function H_4 defined at the centroid (node 4) of the element in the natural coordinate system rst [21] as follows

$$\begin{aligned}
&H_4 = 27rs(1-r-s) \\
&H_1 = 1 - r - s - H_4/3; \quad H_2 = r - H_4/3; \quad H_3 = s - H_4/3
\end{aligned} \tag{10}$$

Owing to the cubic bubble function at the centroid, the strain fields of the 3-node triangular element are enriched and non-constant on each element. As a result, the strain fields on plate structures are smoother than those given by the standard 3-node triangular element. Particularly, from the displacement approximations in Eq. (9), the strain fields in Eq. (6) can be expressed in terms of the nodal displacements by

$$\begin{aligned}
&\boldsymbol{\varepsilon}_m = \sum_{I=1}^{4} \mathbf{B}_I^m \mathbf{u}_I; \quad \boldsymbol{\varepsilon}_b = \sum_{I=1}^{4} \mathbf{B}_I^b \mathbf{u}_I; \quad \boldsymbol{\varepsilon}_\kappa = \sum_{I=1}^{4} \mathbf{B}_I^\kappa \mathbf{u}_I \\
&\boldsymbol{\gamma}_0 = \sum_{I=1}^{4} \mathbf{B}_I^0 \mathbf{u}_I; \quad \boldsymbol{\gamma}_1 = \sum_{I=1}^{4} \mathbf{B}_I^1 \mathbf{u}_I
\end{aligned} \tag{11}$$

in which $\mathbf{u}_I = \begin{bmatrix} u_{0I} & v_{0I} & w_{0I} & \theta_{xI} & \theta_{yI} & \beta_{xI} & \beta_{yI} \end{bmatrix}^T$ is the degrees of freedom at node I; and the gradient matrices are

$$\mathbf{B}_I^m = \begin{bmatrix} H_{I,x} & 0 & 0 & 0 & 0 & 0 \\ 0 & H_{I,y} & 0 & 0 & 0 & 0 \\ H_{I,y} & H_{I,x} & 0 & 0 & 0 & 0 \end{bmatrix}; \quad \mathbf{B}_I^b = \begin{bmatrix} 0 & 0 & 0 & H_{I,x} & 0 & 0 \\ 0 & 0 & 0 & 0 & H_{I,y} & 0 \\ 0 & 0 & 0 & H_{I,y} & H_{I,x} & 0 \end{bmatrix}$$
$$\mathbf{B}_I^\kappa = \begin{bmatrix} 0 & 0 & 0 & H_{I,x} & 0 & H_{I,x} & 0 \\ 0 & 0 & 0 & 0 & H_{I,y} & 0 & H_{I,y} \\ 0 & 0 & 0 & H_{I,y} & H_{I,x} & H_{I,y} & H_{I,x} \end{bmatrix} \tag{12}$$

$$\mathbf{B}_I^0 = \begin{bmatrix} 0 & 0 & H_{I,x} & H_I & 0 & 0 & 0 \\ 0 & 0 & H_{I,y} & 0 & H_I & 0 & 0 \end{bmatrix}; \quad \mathbf{B}_I^1 = 3c \begin{bmatrix} 0 & 0 & 0 & H_I & 0 & H_I & 0 \\ 0 & 0 & 0 & 0 & H_I & 0 & H_I \end{bmatrix} \tag{13}$$

The transverse shear strains $\boldsymbol{\gamma}_0$ in Eq. (11) directly computed from the C^0-type displacements given by Eq. (9) cannot yield a zero value. It leads to an over-forecasting of the transverse shear strains in FG plates when their thickness becomes thin, which is known as the shear-locking phenomenon. To make the presented element effectively usable for both thin and thick FG plates, the transverse shear strains, $\begin{bmatrix} \hat{\gamma}_0^{rt} & \hat{\gamma}_0^{st} \end{bmatrix}^T$, in the natural coordinate system are interpolated again based on the MITC3+ shear removal technique suggested by Lee et al. [21] as follows

$$\begin{aligned} \hat{\gamma}_0^{rt} &= \frac{2}{3}\left(\gamma_{0(B)}^{rt} - \frac{1}{2}\gamma_{0(B)}^{st}\right) + \frac{1}{3}\left(\gamma_{0(C)}^{rt} + \gamma_{0(C)}^{st}\right) + \frac{1}{3}\left[\left(\gamma_{0(F)}^{rt} - \gamma_{0(D)}^{rt}\right) - \left(\gamma_{0(F)}^{st} + \gamma_{0(E)}^{st}\right)\right](3s-1) \\ \hat{\gamma}_0^{st} &= \frac{2}{3}\left(\gamma_{0(A)}^{rt} - \frac{1}{2}\gamma_{0(A)}^{st}\right) + \frac{1}{3}\left(\gamma_{0(C)}^{rt} + \gamma_{0(C)}^{st}\right) + \frac{1}{3}\left[\left(\gamma_{0(F)}^{rt} - \gamma_{0(D)}^{rt}\right) - \left(\gamma_{0(F)}^{st} + \gamma_{0(E)}^{st}\right)\right](3r-1) \end{aligned} \tag{14}$$

in which $\gamma_{0(*)}^{rt}, \gamma_{0(*)}^{st}$ represent the transverse shear strains in the natural coordinate system, which are directly determined from displacement approximations by Eq. (11) at the typing points (*) with their respective coordinates $(A) = (1/6, 2/3), (B) = (2/3, 1/6), (C) = (1/6, 1/6), (D) = (1/3 + 10^{-4}, 1/3 - 2 \times 10^{-4}), (E) = (1/3 - 2 \times 10^{-4}, 1/3 + 10^{-4}), (F) = (1/3 + 10^{-4}, 1/3 + 10^{-4})$ [21].

As a result, the transverse shear strains $\boldsymbol{\gamma}_0$ in Eq. (11) are rewritten in terms of the nodal displacements using the MITC3+ shear-locking removal technique outlined in Eq. (14) by

$$\hat{\boldsymbol{\gamma}}_0 = \sum_{I=1}^{4} \hat{\mathbf{B}}_I^0 \mathbf{u}_I \tag{15}$$

To HSDT-type FG plates under thermo-mechanical loading, the weak form is

$$\begin{aligned} &\sum_{e=1}^{N_e}\left(\int_{\Omega_e} \delta\begin{bmatrix}\boldsymbol{\varepsilon}_m^T & \boldsymbol{\varepsilon}_b^T & \boldsymbol{\varepsilon}_\kappa^T\end{bmatrix}^T \breve{\mathbf{E}} \begin{bmatrix}\boldsymbol{\varepsilon}_m^T & \boldsymbol{\varepsilon}_b^T & \boldsymbol{\varepsilon}_\kappa^T\end{bmatrix} \mathrm{d}\Omega + \int_{\Omega_e} \delta\begin{bmatrix}\hat{\boldsymbol{\gamma}}_0^T & \boldsymbol{\gamma}_1^T\end{bmatrix}^T \breve{\mathbf{G}} \begin{bmatrix}\hat{\boldsymbol{\gamma}}_0^T & \boldsymbol{\gamma}_1^T\end{bmatrix} \mathrm{d}\Omega\right) \\ &= \sum_{e=1}^{N_e}\left(\int_{\Omega_e} \delta w p \mathrm{d}\Omega + \int_{\Omega_e} \delta\begin{bmatrix}\boldsymbol{\varepsilon}_m^T & \boldsymbol{\varepsilon}_b^T & \boldsymbol{\varepsilon}_\kappa^T\end{bmatrix}^T \begin{bmatrix}\mathbf{N}_{th}^T & \mathbf{M}_{th}^T & \mathbf{P}_{th}^T\end{bmatrix} \mathrm{d}\Omega\right) \end{aligned} \tag{16}$$

where N_e is the number of elements; Ω_e is the domain of an element; and

$$\mathbf{N}_{th} = \int_{-t/2}^{t/2} \alpha(z)\,\Delta T(z)\,\mathbf{E}[1\ \ 1\ \ 0]^T \mathrm{d}z;\quad \mathbf{M}_{th} = \int_{-t/2}^{t/2} \alpha(z)\,\Delta T(z)\,z\mathbf{E}[1\ \ 1\ \ 0]^T \mathrm{d}z$$
$$\mathbf{P}_{th} = \int_{-t/2}^{t/2} \alpha(z)\,\Delta T(z)\,z^3\mathbf{E}[1\ \ 1\ \ 0]^T \mathrm{d}z \tag{17}$$

$$\breve{\mathbf{E}} = \begin{bmatrix} \bar{\mathbf{A}} & \bar{\mathbf{B}} & \bar{\mathbf{E}} \\ \bar{\mathbf{B}} & \bar{\mathbf{D}} & \bar{\mathbf{F}} \\ \bar{\mathbf{E}} & \bar{\mathbf{F}} & \bar{\mathbf{H}} \end{bmatrix};\quad \breve{\mathbf{G}} = \begin{bmatrix} \bar{\mathbf{A}}_s & \bar{\mathbf{B}}_s \\ \bar{\mathbf{B}}_s & \bar{\mathbf{D}}_s \end{bmatrix} \tag{18}$$

with

$$\left(\bar{\mathbf{A}}, \bar{\mathbf{B}}, \bar{\mathbf{D}}, \bar{\mathbf{E}}, \bar{\mathbf{F}}, \bar{\mathbf{H}}\right) = \int_{-t/2}^{t/2} \left(1, z, z^2, z^3, z^4, z^6\right)\mathbf{E}\mathrm{d}z;\quad \left(\bar{\mathbf{A}}_s, \bar{\mathbf{B}}_s, \bar{\mathbf{D}}_s\right) = \int_{-t/2}^{t/2} \left(1, z^2, z^4\right)\mathbf{G}\mathrm{d}z \tag{19}$$

By substituting the relations between the strains and nodal displacements given in Eqs. (11) and (15) into the weak form in (16) and following the standard FEM procedure, the discretized equilibrium equations can be obtained as follows

$$\sum_{e=1}^{N_e} \mathbf{k}^e \mathbf{u}^e = \sum_{e=1}^{N_e} \mathbf{f}^e \tag{20}$$

wherein, $\mathbf{u}^e = \left[\mathbf{u}_1^T\ \ \mathbf{u}_2^T\ \ \mathbf{u}_3^T\ \ \mathbf{u}_4^T\right]^T$;

$$\mathbf{k}_{IJ}^e = \int_{\Omega_e} \left(\mathbf{B}_I^T \breve{\mathbf{E}} \mathbf{B}_J + \mathbf{B}_{sI}^T \breve{\mathbf{G}} \mathbf{B}_{sJ}\right)\mathrm{d}\Omega;\quad \mathbf{f}_I^e = \int_{\Omega_e} [0\ \ 0\ \ H_I\ \ 0\ \ 0\ \ 0\ \ 0]^T p\mathrm{d}\Omega + \int_{\Omega_e} \mathbf{B}_I^T \left[\mathbf{N}_{th}^T\ \ \mathbf{M}_{th}^T\ \ \mathbf{P}_{th}^T\right]\mathrm{d}\Omega \tag{21}$$

with

$$\mathbf{B}_I = \left[\left(\mathbf{B}_I^m\right)^T \left(\mathbf{B}_I^b\right)^T \left(\mathbf{B}_I^\kappa\right)^T\right]^T;\quad \mathbf{B}_{sI} = \left[\left(\hat{\mathbf{B}}_I^0\right)^T \left(\mathbf{B}_I^1\right)^T\right]^T \tag{22}$$

2.2. Cell-based smoothed (CS) MITC3+ plate element for HSDT-type FG plates

To smooth the strain fields of plates discretized by 3-node triangular elements, the strain fields on adjacent elements are averaged using the ES- or NS-FEM. However, these approaches require additional computational time to identify elements with common edges or nodes. In this study, the in-plane strains of the MITC3+ plate element, which are not constant on the element domain, are averaged over sub-domains based on the CS-FEM [14] to transform surface integration of the element stiffness matrices in Eq. (21) to line integration. The cell-based smoothed method is directly implemented within each iteration of computing element stiffness matrices. Specifically, the 3-node triangular MITC3+ plate element is divided into 3 sub-triangular domains by straight lines connecting the vertex nodes to the bubble node. The in-plane strains in each sub-triangular domain Ω_{SC} with the area A_{SC} are smoothed by

$$\tilde{\boldsymbol{\varepsilon}}_m = \frac{1}{A_{SC}} \int_{\Omega_{SC}} \boldsymbol{\varepsilon}_m \mathrm{d}\Omega;\quad \tilde{\boldsymbol{\varepsilon}}_b = \frac{1}{A_{SC}} \int_{\Omega_{SC}} \boldsymbol{\varepsilon}_b \mathrm{d}\Omega;\quad \tilde{\boldsymbol{\varepsilon}}_\kappa = \frac{1}{A_{SC}} \int_{\Omega_{SC}} \boldsymbol{\varepsilon}_\kappa \mathrm{d}\Omega \tag{23}$$

By applying Green's theorem to the surface integrations of the shape function derivatives and using 2 Gaussian quadrature points to compute the line integrations, the following terms are determined

$$\begin{aligned}\tilde{H}_{Ix} &= \int_{\Omega_{SC}} H_{I,x}\mathrm{d}A = \sum_{ed=1}^{3}\int_{L_{ed}} H_I n_x \mathrm{d}L = \sum_{ed=1}^{3}\sum_{qp=1}^{2} H_I^{qp} W^{qp} n_x^{ed} \\ \tilde{H}_{Iy} &= \int_{\Omega_{SC}} H_{I,y}\mathrm{d}A = \sum_{ed=1}^{3}\int_{L_{ed}} H_I n_y \mathrm{d}L = \sum_{ed=1}^{3}\sum_{qp=1}^{2} H_I^{qp} W^{qp} n_y^{ed}\end{aligned} \tag{24}$$

in which L_{ed} is the length of each edge of the sub-triangular domain Ω_{SC}; n_x^{ed} and n_y^{ed} are respectively the x- and y-direction components of vector normal to edge ed of the domain Ω_{SC}; H_I^{qp} are the values of the shape functions evaluated at Gaussian quadrature points qp with their weight W^{qp}.

Substituting the relationship between the in-plane strains and the nodal displacements given in Eq. (11) into Eq. (23) and employing the results in Eq. (24), the in-plane smoothed strains in Eq. (23) can be expressed as follows

$$\tilde{\boldsymbol{\varepsilon}}_m = \sum_{I=1}^{4} \tilde{\mathbf{B}}_I^m \mathbf{u}_I; \quad \tilde{\boldsymbol{\varepsilon}}_b = \sum_{I=1}^{4} \tilde{\mathbf{B}}_I^b \mathbf{u}_I; \quad \tilde{\boldsymbol{\varepsilon}}_\kappa = \sum_{I=1}^{4} \tilde{\mathbf{B}}_I^\kappa \mathbf{u}_I \tag{25}$$

where

$$\begin{aligned}\tilde{\mathbf{B}}_I^m &= \begin{bmatrix} \tilde{H}_{Ix} & 0 & 0 & 0 & 0 & 0 \\ 0 & \tilde{H}_{Iy} & 0 & 0 & 0 & 0 \\ \tilde{H}_{Iy} & \tilde{H}_{Ix} & 0 & 0 & 0 & 0 \end{bmatrix}; \quad \tilde{\mathbf{B}}_I^b = \begin{bmatrix} 0 & 0 & 0 & \tilde{H}_{Ix} & 0 & 0 \\ 0 & 0 & 0 & 0 & \tilde{H}_{Iy} & 0 \\ 0 & 0 & 0 & \tilde{H}_{Iy} & \tilde{H}_{Ix} & 0 \end{bmatrix} \\ \tilde{\mathbf{B}}_I^\kappa &= \begin{bmatrix} 0 & 0 & 0 & \tilde{H}_{Ix} & 0 & \tilde{H}_{Ix} & 0 \\ 0 & 0 & 0 & 0 & \tilde{H}_{Iy} & 0 & \tilde{H}_{Iy} \\ 0 & 0 & 0 & \tilde{H}_{Iy} & \tilde{H}_{Ix} & \tilde{H}_{Iy} & \tilde{H}_{Ix} \end{bmatrix}\end{aligned} \tag{26}$$

As a result, the formulation of the CS-MITC3+ plate element for the HSDT-type FG plates can be derived from the stiffness of the MITC3+ plate element given in Eq. (21) as follows

$$\tilde{\mathbf{k}}_{IJ}^e = \sum_{sc=1}^{3} \left[\left(\tilde{\mathbf{B}}_I^m\right)_{SC}^T \quad \left(\tilde{\mathbf{B}}_I^b\right)_{SC}^T \quad \left(\tilde{\mathbf{B}}_I^\kappa\right)_{SC}^T \right]^T \mathbf{E} \left[\left(\tilde{\mathbf{B}}_J^m\right)_{SC} \quad \left(\tilde{\mathbf{B}}_J^b\right)_{SC} \quad \left(\tilde{\mathbf{B}}_J^\kappa\right)_{SC} \right] A_{SC} + \int_{\Omega_e} \mathbf{B}_{sI}^T \breve{\mathbf{G}} \mathbf{B}_{sJ} \mathrm{d}\Omega \tag{27}$$

The displacements of the bubble node (node 4) are eliminated by applying the condensation technique to the equilibrium equations $\tilde{\mathbf{k}}^e \mathbf{u}^e = \mathbf{f}^e$ to construct the formulation of the stiffness matrix and force vector of the CS-MITC3+ plate element, involving only nodal displacements at the vertex nodes. Subsequently, the discretized equilibrium equations of the FG plates are obtained

$$\mathbf{K}\mathbf{U} = \mathbf{F} \tag{28}$$

in which $\mathbf{U}$ represents the nodal displacements of all nodes in the FG plates, while $\mathbf{K}$ and $\mathbf{F}$ denote the plate's stiffness matrix and force vector, respectively, assembled from the element stiffness matrices and force vectors.

3. Numerical investigations

In this section, the effectiveness of the suggested CS-MITC3+ plate element is assessed through static analysis of various benchmark FG plates. The properties of FG ingredients are listed in Table 1.

Table 1. Ingredient properties of FG plates

	Al	Al_2O_3	ZrO_2-1	ZrO_2-2
E (GPa)	70	380	200	151
ν	0.3	0.3	0.3	0.3
k (W/mK)	204	10.4	2.09	2.09
α ($\times 10^{-6}$/°C)	23	7.2	10	10

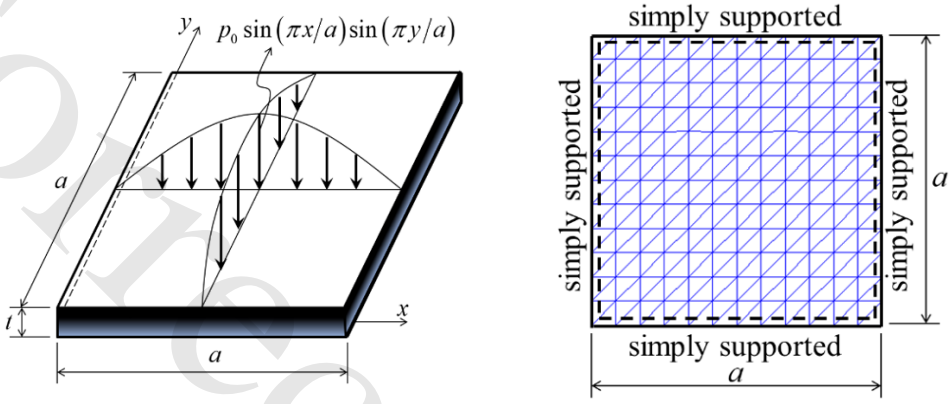

(a) Subjected to sinusoidal load

(b) Discretized by a regular mesh of 12×12×2 three-node triangular elements

Figure 3. Geometry of a simply supported FG plate

3.1. FG square plates under mechanical loads

A simply supported square plate of length a and thickness t is subjected to sinusoidal load $p = p_0 \sin(\pi x/a)\sin(\pi y/a)$ as depicted in Fig. 3(a). The plate is made of Al and Al_2O_3 materials. To compare with reference results, the deflection w_c at the plate center and stresses σ_{xx}, τ_{xy}, τ_{xz} are normalized by

$$\bar{w}_c = \frac{10 w_c E_c t^3}{p_0 a^4}; \quad \bar{\sigma}_{xx}(z) = \frac{t}{p_0 a}\sigma_{xx}\left(\frac{a}{2}, \frac{a}{2}, z\right)$$
$$\bar{\tau}_{xy}(z) = \frac{t}{p_0 a}\tau_{xy}(0,0,z); \quad \bar{\tau}_{xz}(z) = \frac{t}{p_0 a}\tau_{xz}\left(0, \frac{a}{2}, z\right) \tag{29}$$

To study the convergence rate of the proposed element, the plate with $a/t = 10$ is simulated by regular meshes of 12×12×2, 16×16×2, 20×20×2, or 24×24×2 three-node triangular elements. Fig. 3(b) illustrates the 12×12×2 mesh. The relative errors $\left|w_c - w_c^{ref}\right|/w_c^{ref}$ and $\left|\sigma_{xx} - \sigma_{xx}^{ref}\right|/\sigma_{xx}^{ref}$ at $z = t/3$, in which w_c, σ_{xx}, w_c^{ref}, σ_{xx}^{ref} are respectively the deflections and normal stresses at the plate's center predicted by the different sizes of the CS-MITC3+ plate elements and the HSDT analytical solutions [29], are graphed in the logarithmic scales in Fig. 4. For the various power law indices $n = 1, 2, 4, 8$ and 10, the CS-MITC3+ plate element well converges to the analytical solutions. With the 24×24×2 mesh, the relative errors are about 0.5% and 1.0% for the central deflections w_c and the normal stresses σ_{xx} at the point $(a/2, a/2, t/3)$. Therefore, the mesh of 24×24×2 elements is used to obtain the numerical results of the CS-MITC3+ plate element in this study. Owing to the HSDT, the normalized shear stresses $\bar{\tau}_{xy}$ at point $(0, 0)$ and $\bar{\tau}_{xz}$ at point $(0, a/2)$ provided by the CS-MITC3+ plate element cubically vary through the thickness and are similar to those given by the analytical

solutions [29] for $n = 1$ and 8 as demonstrated in Fig. 5. The transverse shear stresses vanish at the bottom and top planes of the plate.

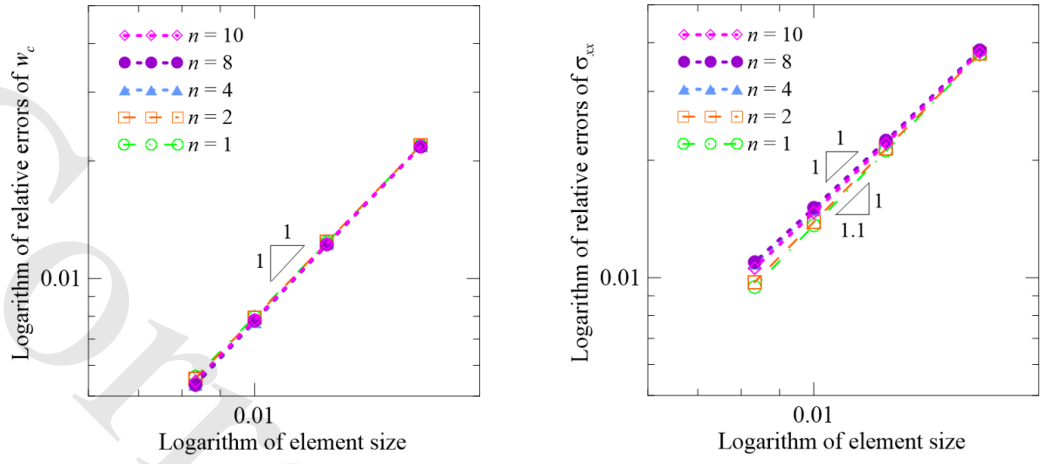

(a) The central deflections wc (b) The normal stresses $\sigma_{xx}(a/2, a/2, t/3)$

Figure 4. Convergence rates given by the CS-MITC3+ plate element as compared with the HSDT analytical solutions [29] for the Al/Al_2O_3 plates under the sinusoidal load

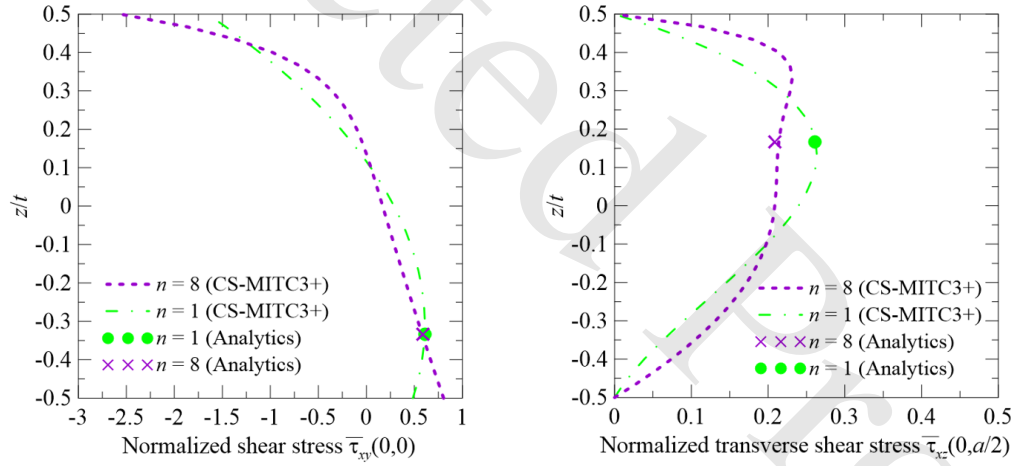

(a) (b)

Figure 5. Variation of the normalized shear stresses through the thickness of the Al/Al_2O_3 plate with $a/t = 10$ under the sinusoidal load

Table 2 lists the normalized deflections and stresses at the plate's center determined by the CS-MITC3+ plate element for the Al/Al_2O_3 plates with $a/t = 4$, 10 and 100. For both thick and thin plates, these numerical results are in good agreement with those given by the HSDT analytical solution [29], the CS-DSG3 element [17], and the quasi-3D HSDT meshless method [30]. This means that the presented elements can overcome the shear-locking phenomenon. Table 2 also shows the effect of the power law index on the behaviors of FG plates. When the power law index or the percentage of the Al ingredient increases, the deflections increase and the stresses decrease, or the FG plates become softer.

Table 2. Normalized central deflections and stresses at the point $(a/2, a/2, t/3)$ of the Al/Al_2O_3 plates under the sinusoidal load

a/t	Methods	$n = 1$		$n = 4$		$n = 10$	
		$\bar{w}_c$	$\bar{\sigma}_{xx}$	$\bar{w}_c$	$\bar{\sigma}_{xx}$	$\bar{w}_c$	$\bar{\sigma}_{xx}$
4	CS-MITC3+	0.7246	0.5762	1.1544	0.4374	1.3835	0.3209
	CS-DSG3 [17]	0.7240	0.5761	1.1539	0.4371	1.3831	0.3207
	Analytics [29]	0.7284	0.5812	1.1599	0.4449	1.3909	0.3259
	Meshless [30]	0.7020	0.5911	1.1108	0.4330	1.3334	0.3097
10	CS-MITC3+	0.5857	1.4757	0.8768	1.1666	1.0032	0.8692
	CS-DSG3 [17]	0.5851	1.4757	0.8760	1.1665	1.0023	0.8691
	Analytics [29]	0.5890	1.4898	0.8815	1.1794	1.0087	0.8785
	Meshless [30]	0.5913	1.4874	0.8770	1.1592	0.9952	0.8468
100	CS-MITC3+	0.5594	14.8243	0.8240	11.8069	0.9309	8.8209
	CS-DSG3 [17]	0.5586	14.8218	0.8229	11.8051	0.9298	8.8198
	Analytics [29]	0.5625	14.9676	0.8287	11.9209	0.9362	8.9060
	Meshless [30]	0.5648	14.9440	0.8241	11.7370	0.9228	8.6011

The FG square plates are now subjected to uniformly distributed load p_0 and composed of Al and ZrO_2-1. With the mesh of $24 \times 24 \times 2$ CS-MITC3+ plate elements, the normalized central deflections $\bar{w}_c = 100 w_c E_m t^3/[12(1-\nu^2)p_0 a^4]$ of the Al/ZrO_2-1 square plates with $a/t = 5$ and $n = 0$, 0.5, 1, 2 are given in Table 3 for both simply supported and clamped plate cases. The results are similar to those provided by the CS-DSG3 element [17], isogeometric analysis (IGA) [31] or meshless local Petrov-Galerkin (MLPG) method [32]. Fig. 4(a) illustrates the distributions of thickness-through normalized normal stresses $\bar{\sigma}_{xx} = t^2\sigma_{xx}/(p_0 a^2)$ at the plate center for simple supports, while Fig. 4(b) presents them for clamped supports, as obtained by the CS-MITC3+ plate element. Fig. 4 shows the excellent agreement of the normalized normal stresses predicted by the presented element and the MLPG method [32] in the investigated studies of $n = 0$ and 2.

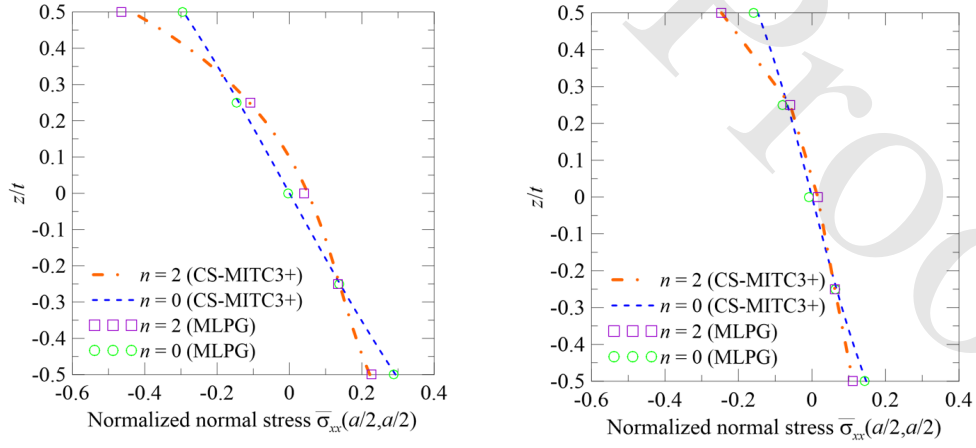

(a) Simple support (b) Clamped support

Figure 6. Variation of the normalized normal stresses through the thickness of the Al/ZrO_2-1 plate with $a/t = 5$ under the uniformly distributed load

Table 3. Normalized central deflections $\bar{w}_c$ of the Al/ZrO_2-1 plates with $a/t = 5$ under the uniformly distributed load

Boundaries	Methods	$n = 0$	$n = 0.5$	$n = 1$	$n = 2$
Simply	CS-MITC3+	0.1709	0.2310	0.2707	0.3122
	CS-DSG3 [17]	0.1774	0.2343	0.2688	0.3060
	IGA [31]	0.1717	0.2324	0.2719	0.3115
	MLPG [32]	0.1657	0.2482	0.2878	0.3251
Clamped	CS-MITC3+	0.0749	0.0995	0.1166	0.1368
	CS-DSG3 [17]	0.0732	0.0972	0.1139	0.1336
	IGA [31]	0.0760	0.1014	0.1183	0.1369
	MLPG [32]	0.0729	0.1069	0.1248	0.1438

3.2. Al/ZrO_2-1 skew plates under uniformly distributed load

A skew plate shown in Fig. 7 has the length of each edge a, thickness $t = a/100$, and skew angle α. The FG materials of the plate include Al and ZrO_2-1. The plate is simply supported on all edges and applied uniformly distributed load p_0.

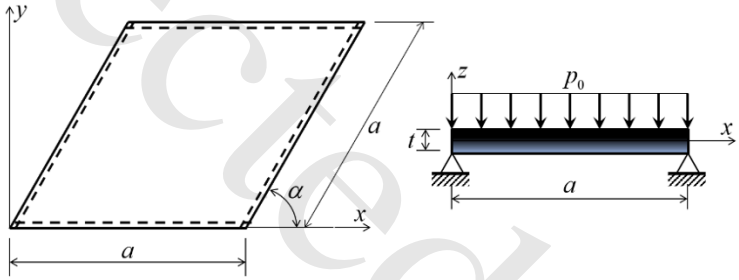

Figure 7. Geometry of Al/ZrO_2-1 skew plate under uniformly distributed load

The FG skew plate is discretized by the regular mesh of 24×24×2 CS-MITC3+ plate elements. The normalized deflections $\bar{w}_c = 100 w_c E_c t^3 / \left[12\left(1-\nu^2\right) p_0 a^4\right]$ at the plate center with various values of the skew angles α and power law indices n are plotted in Fig. 8. The numerical results in Fig. 8 indicate that the rigidity of the FG plates decreases as the power law indices increase because of the reduction in the ceramic content. When the skew angle increases, the span of the plate also increases, leading to an increase in the central deflections as demonstrated in Fig. 8. The thickness-through distributions of the normalized normal stresses $\bar{\sigma}_{xx} = t^2 \sigma_{xx} / \left(p_0 a^2\right)$ at the plate center given by the proposed element are illustrated in Fig. 9 for different skew angles and for $n = 0.5$ and 2. These results are in excellent agreement with those obtained by the CS-DSG3 element [17].

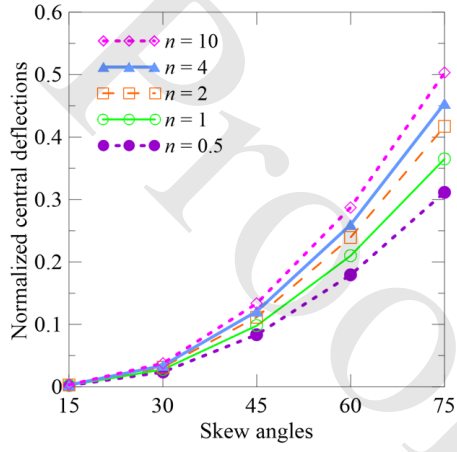

Figure 8. Normalized central deflections of the simply supported Al/ZrO_2-1 skew plate under uniformly distributed load in the different cases of the skew angles α and power law indices n

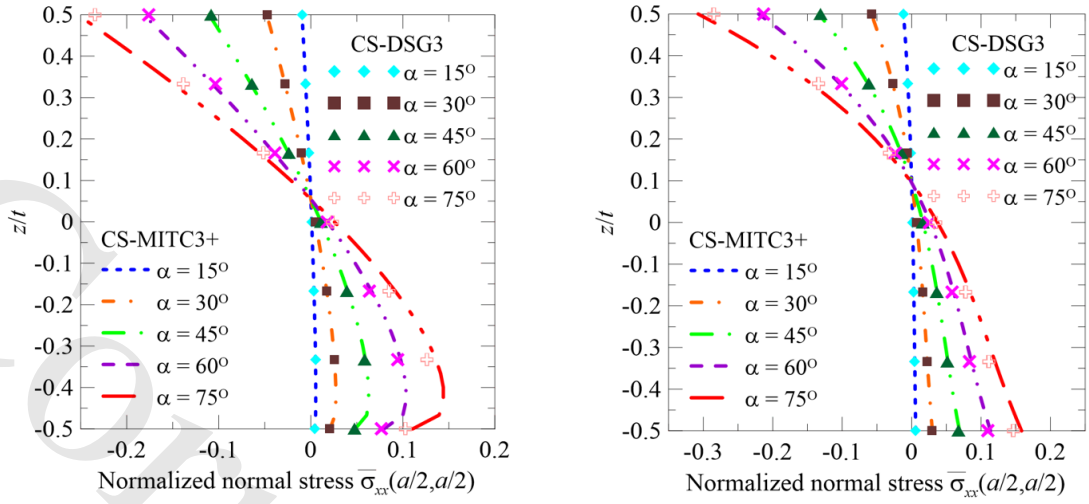

(a) $n = 0.5$ (b) $n = 2$

Figure 9. Distribution of the normalized normal stresses $\bar{\sigma}_{xx}$ at the center of the simply supported Al/ZrO_2-1 plate under uniformly distributed load with various skew angles α and power law indices (a) $n = 0.5$ and (b) $n = 2$

3.3. Al/ZrO_2-2 square plates under thermo-mechanical load

A functionally graded square plate made of aluminum (Al) at the bottom plane and zirconia (ZrO_2-2) at the top plane is considered. The FG plate of the length $a = 0.2$ m and thickness $t = 0.01$ m is simply supported on all edges. The plate is subjected to thermo-mechanical load, including temperature T_m on the bottom plane, T_c on the top plane, and uniformly distributed load $p_0 = lf \times E_m \times t^4/a^4$ on the top plane. The plate is modeled by the regular mesh of $24 \times 24 \times 2$ CS-MITC3+ plate elements to obtain the normalized deflections w_c/t at the plate center.

Firstly, the Al/ZrO_2-2 square plate is purely applied temperature $T_m = 20$ °C and $T_c = 0$ °C, 100 °C, 200 °C, 300 °C, 400 °C or 500 °C. Fig. 10 demonstrates the variation of the normalized deflections computed by the CS-MITC3+ plate element as the temperature difference between the bottom and top planes and the power law indices increase. The thermal loads cause the FG plate to deform upward. The deflections tend to significantly increase when the power law indices, meaning the aluminum content, are large because the thermal conductivity of the metal is greater than that of ceramics.

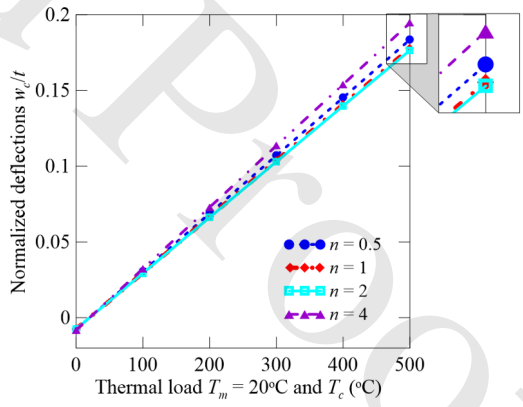

Figure 10. Normalized central deflections of the Al/ZrO_2-2 square plate due to variety of thermal loads

Secondly, the FG square plate is subjected to both the thermal load of $T_m = 20$ °C and $T_c = 300$ °C, and the uniformly distributed load $p_0 = lf \times E_m \times t^4/a^4$, in which lf denotes the load factor, with the negative sign indicating the downward direction of the load. Fig. 11 represents the normalized deflections at the plate center given by the CS-MITC3+ and CS-DSG3 elements in the various cases of the load factor $lf = 0, -2, -4, -6, -8,$

-10, -12, 14 and the power law indices $n = 0.5$, 1, 2, 4. The numerical results of the CS-MITC3+ and CS-DSG3 elements are the same. When the mechanical loads increase, the deflections of the Al/ZrO_2-2 plate change from upward to downward directions as demonstrated in Fig. 12 for the case $lf = -8$ and $n = 2$. It can be observed that the thermo-mechanical loading reduces the deflections of the FG plate compared to the case of purely mechanical load.

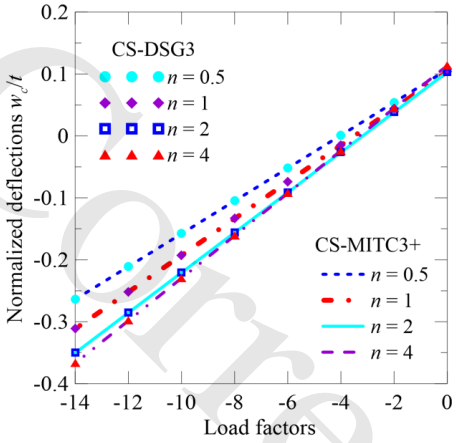

Figure 11. Normalized central deflections of the Al/ZrO_2-2 square plate due to variety of mechanical loads and thermal load of $T_m = 20^\circ$ and $T_c = 300^\circ$

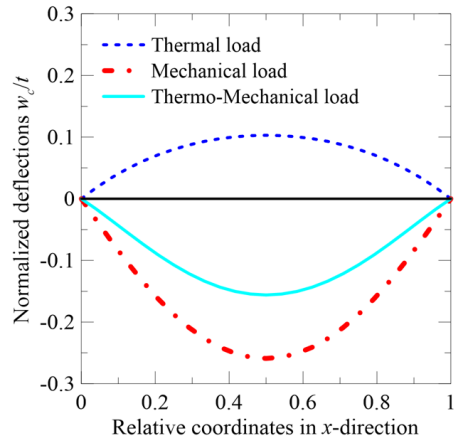

Figure 12. Normalized deflections at central line of the Al/ZrO_2-2 square plate due to thermal, mechanical and thermo-mechanical loads

4. Conclusions

Using HSDT and cell-based smoothed FEM, a 3-node triangular plate element has been developed for the static analysis of FG plates. The presented element utilizes C0-type shape functions enriched by adding a cubic function at the bubble node. The in-plane strains are smoothed over sub-triangular domains defined by the vertex and bubble nodes. Meanwhile, the transverse shear strains are re-interpolated using the MITC3+ technique to mitigate the shear-locking phenomenon. The numerical results for the investigated FG plates with various geometries, boundary conditions, loads and exponent law indices show that the proposed CS-MITC3+ plate element can predict defections and stresses in excellent agreement with methods such as analytical solutions, the CS-DSG3 element, meshless approaches, or IGA. When subjected to both thermal and mechanical loadings, the FG plates exhibit superior performance, as they reduce deflections and stresses compared to cases subjected to only thermal or mechanical loadings.

Acknowledgements

This work belongs to the project grant No: T2024-78 funded by Ho Chi Minh City University of Technology and Education, Vietnam.

References

[1] Koizumi, M. (1997). FGM activities in Japan. *Composites Part B: Engineering*, 28(1–2):1–4.
[2] Timoshenko, S. P., Woinowsky-Krieger, S. (1959). *Theory of plates and shells*. Second edition, McGraw-Hill.
[3] Reissner, E. (1945). The effect of transverse shear deformation on the bending of elastic plates. *Journal of Applied Mechanics*, 12(2):A69–A77.
[4] Mindlin, R. D. (1951). Influence of rotatory inertia and shear on flexural motions of isotropic, elastic plates. *Journal of Applied Mechanics*, 18(1):31–38.

[5] Reddy, J. N. (2000). Analysis of functionally graded plates. *International Journal for Numerical Methods in Engineering*, 47(1-3):663–684.
[6] Thai, H.-T., Vo, T. P. (2013). A new sinusoidal shear deformation theory for bending, buckling, and vibration of functionally graded plates. *Applied Mathematical Modelling*, 37(5):3269–3281.
[7] Xiang, S., Kang, G.-w. (2013). A nth-order shear deformation theory for the bending analysis on the functionally graded plates. *European Journal of Mechanics - A/Solids*, 37:336–343.
[8] Nguyen, V.-H., Nguyen, T.-K., Thai, H.-T., Vo, T. P. (2014). A new inverse trigonometric shear deformation theory for isotropic and functionally graded sandwich plates. *Composites Part B: Engineering*, 66: 233–246.
[9] Van, V. T., Hieu, N. V. (2022). Buckling analysis of functionally graded sandwich plates resting on Pasternak foundation using a novel refined quasi-3D third-order shear deformation theory. *Journal of Science and Technology in Civil Engineering (STCE) - HUCE*, 16(1):68–79.
[10] Son, T. (2025). Geometrically nonlinear analysis of functionally graded plates with symmetrical parabolic thickness profile under uniaxial compression based on isogeometric analysis. *Journal of Science and Technology in Civil Engineering (JSTCE) - HUCE*, 19(1):59–71.
[11] Tessler, A., Hughes, T. J. (1985). A three-node Mindlin plate element with improved transverse shear. *Computer Methods in Applied Mechanics and Engineering*, 50(1):71–101.
[12] Bletzinger, K.-U., Bischoff, M., Ramm, E. (2000). A unified approach for shear-locking-free triangular and rectangular shell finite elements. *Computers & Structures*, 75(3):321–334.
[13] Lee, P.-S., Bathe, K.-J. (2004). Development of MITC isotropic triangular shell finite elements. *Computers & Structures*, 82(11–12):945–962.
[14] Liu, G. R., Nguyen-Thoi, T. (2010). *Smoothed finite element methods*. CRC Press.
[15] Nguyen-Xuan, H., Tran, L. V., Nguyen-Thoi, T., Vu-Do, H. (2011). Analysis of functionally graded plates using an edge-based smoothed finite element method. *Composite Structures*, 93(11):3019–3039.
[16] Nguyen-Xuan, H., Tran, L. V., Thai, C. H., Nguyen-Thoi, T. (2012). Analysis of functionally graded plates by an efficient finite element method with node-based strain smoothing. *Thin-Walled Structures*, 54:1–18.
[17] Phung-Van, P., Nguyen-Thoi, T., Tran, L. V., Nguyen-Xuan, H. (2013). A cell-based smoothed discrete shear gap method (CS-DSG3) based on the C0-type higher-order shear deformation theory for static and free vibration analyses of functionally graded plates. *Computational Materials Science*, 79:857–872.
[18] Phung-Van, P., Nguyen-Thoi, T., Luong-Van, H., Lieu-Xuan, Q. (2014). Geometrically nonlinear analysis of functionally graded plates using a cell-based smoothed three-node plate element (CS-MIN3) based on the C0-HSDT. *Computer Methods in Applied Mechanics and Engineering*, 270:15–36.
[19] Nguyen, T.-K., Nguyen, V.-H., Chau-Dinh, T., Vo, T. P., Nguyen-Xuan, H. (2016). Static and vibration analysis of isotropic and functionally graded sandwich plates using an edge-based MITC3 finite elements. *Composites Part B: Engineering*, 107:162–173.
[20] Nguyen, T.-K., Nguyen, V.-H., Chau-Dinh, T. (2018). Cell- and Node-Based Smoothing MITC3-Finite Elements for Static and Free Vibration Analysis of Laminated Composite and Functionally Graded Plates. *International Journal of Computational Methods*, 16(08):1850123.
[21] Lee, Y., Lee, P.-S., Bathe, K.-J. (2014). The MITC3+ shell element and its performance. *Computers & Structures*, 138:12–23.
[22] Thanh, C. D., Tuyen, V. N., Phuc, N. H. (2017). A cell-based smoothed three-node plate finite element with a bubble node for static analyses of both thin and thick plates. *Vietnam Journal of Mechanics*, 39(3): 229–243.
[23] Anh, L. T. N., Ninh, V. T. A., Lang, T. V., Kien, N. D. (2020). Free vibration of bidirectional functionally graded sandwich beams using a first-order shear deformation finite element formulation. *Journal of Science and Technology in Civil Engineering (STCE) - NUCE*, 14(3):136–150.
[24] Do, D. T. T. (2024). Ensemble learning methods for the mechanical behavior prediction of tri-directional functionally graded plates. *Journal of Science and Technology in Civil Engineering (JSTCE) - HUCE*, 18 (4):98–108.
[25] Son, T., X. Qui, L. (2022). Investigate the bending and free vibration responses of multi-directional

functionally graded plates with variable thickness based on isogeometric analysis. *Journal of Science and Technology in Civil Engineering (JSTCE) - HUCE*, 16(4):10–29.

[26] Lanhe, W. (2004). Thermal buckling of a simply supported moderately thick rectangular FGM plate. *Composite Structures*, 64(2):211–218.

[27] Reddy, J. N. (2004). *Mechanics of Laminated Composite Plates and Shells - Theory and Analysis*. Second edition, CRC Press.

[28] Shankara, C., Iyengar, N. (1996). A C0 element for the free vibration analysis of laminated composite plates. *Journal of Sound and Vibration*, 191(5):721–738.

[29] Thai, H.-T., Kim, S.-E. (2013). A simple higher-order shear deformation theory for bending and free vibration analysis of functionally graded plates. *Composite Structures*, 96:165–173.

[30] Neves, A., Ferreira, A., Carrera, E., Cinefra, M., Roque, C., Jorge, R., Soares, C. (2013). Static, free vibration and buckling analysis of isotropic and sandwich functionally graded plates using a quasi-3D higher-order shear deformation theory and a meshless technique. *Composites Part B: Engineering*, 44(1): 657–674.

[31] Valizadeh, N., Natarajan, S., Gonzalez-Estrada, O. A., Rabczuk, T., Bui, T. Q., Bordas, S. P. (2013). NURBS-based finite element analysis of functionally graded plates: Static bending, vibration, buckling and flutter. *Composite Structures*, 99:309–326.

[32] Gilhooley, D., Batra, R., Xiao, J., McCarthy, M., Gillespie, J. (2007). Analysis of thick functionally graded plates by using higher-order shear and normal deformable plate theory and MLPG method with radial basis functions. *Composite Structures*, 80(4):539–552.